JOURNAL OF SYNCHROTRON RADIATION
ISSN 1600-5775

Received 2 September 2019
Accepted 18 February 2020

Edited by S. Svensson, Uppsala University, Sweden

Keywords: soft X-ray; scanning spectromicroscope; photon-in/photon-out; low vacuum; helium atmosphere.

Development of a scanning soft X-ray spectromicroscope to investigate local electronic structures on surfaces and interfaces of advanced materials under conditions ranging from low vacuum to helium atmosphere

Masaki Oura,[a]* Tomoko Ishihara,[a] Hitoshi Osawa,[b] Hiroyuki Yamane,[a] Takaki Hatsui[a] and Tetsuya Ishikawa[a]

[a]RIKEN SPring-8 Center, 1-1-1 Kouto, Sayo-cho, Sayo-gun, Hyogo 679-5148, Japan, and [b]JASRI, 1-1-1 Kouto, Sayo-cho, Sayo-gun, Hyogo 679-5198, Japan. *Correspondence e-mail: oura@spring8.or.jp

A scanning soft X-ray spectromicroscope was recently developed based mainly on the photon-in/photon-out measurement scheme for the investigation of local electronic structures on the surfaces and interfaces of advanced materials under conditions ranging from low vacuum to helium atmosphere. The apparatus was installed at the soft X-ray beamline (BL17SU) at SPring-8. The characteristic features of the apparatus are described in detail. The feasibility of this spectromicroscope was demonstrated using soft X-ray undulator radiation. Here, based on these results, element-specific two-dimensional mapping and micro-XAFS (X-ray absorption fine structure) measurements are reported, as well as the observation of magnetic domain structures from using a reference sample of permalloy micro-dot patterns fabricated on a silicon substrate, with modest spatial resolution (*e.g.* ∼500 nm). Then, the X-ray radiation dose for Nafion® near the fluorine *K*-edge is discussed as a typical example of material that is not radiation hardened against a focused X-ray beam, for near future experiments.

1. Introduction

It is widely known that the distribution of molecules adsorbed on a solid surface, even the clean surface of a single crystal in a vacuum, is not homogeneous for heterogeneous catalyst reactions on the surface. Surfaces under atmospheric pressure are much more complicated, but present an intriguing research subject for a realistic view of surface science, by investigating electronic structures on surfaces using both microscopic and spectroscopic methods. For typical surface phenomena, such as physisorption, chemisorption, oxidation reactions and catalytic reactions, oxygen is recognized as one of the most important agents for chemical reactions on surfaces. Therefore, information about local electronic structures around oxygen, or oxygen-containing functional groups, relating to surface chemical reactions is indispensable for understanding such surface phenomena.

Synchrotron-radiation-based soft X-ray (SX) microspectroscopy provides a powerful probe for investigating local electronic structures relating to surface phenomena. To date, extensive work on SX microspectroscopic methods has been made for surface analysis (for example, Günther *et al.*, 2002; Watts & McNeill, 2010; Leung *et al.*, 2010; Kaulich *et al.*, 2011; Abyaneh *et al.*, 2011; Horiba *et al.*, 2011; Hitchcock *et al.*, 2012; Schofield *et al.*, 2014; Guttmann & Bittencourt, 2015, Bozzini

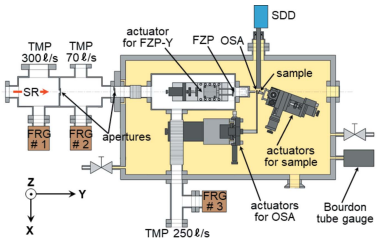

et al., 2015; Ohigashi *et al.*, 2016; Prabu *et al.*, 2018; Leontowich *et al.*, 2018; Lühl *et al.*, 2019). SX spectromicroscopes can be classified into two types depending on their working principles: full-field microscopes and scanning microscopes. In full-field microscopes, *e.g.* transmission X-ray microscopes (TXM) (Kaulich *et al.*, 2011; Guttmann & Bittencourt, 2015) and X-ray photoemission electron microscopes (X-PEEM) (Günther *et al.*, 2002; Leung *et al.*, 2010; Schofield *et al.*, 2014), the whole field of view is directly imaged onto a detector plane so that a spatially resolved imaging detector, such as a CCD or a pixel-array detector, is required. On the other hand, with scanning microscopes, *e.g.* scanning photoelectron microscopes (SPEM) (Günther *et al.*, 2002; Abyaneh *et al.*, 2011; Horiba *et al.*, 2011; Bozzini *et al.*, 2015) and scanning transmission X-ray microscopes (STXM) (Watts & McNeill, 2010; Leung *et al.*, 2010; Kaulich *et al.*, 2011; Hitchcock *et al.*, 2012; Ohigashi *et al.*, 2016; Prabu *et al.*, 2018; Leontowich *et al.*, 2018; Lühl *et al.*, 2019), a focused SX beam is raster-scanned over the sample (actually the sample is two-dimensionally scanned relative to the SX beam) and then each data-point is corrected separately, which results in time-consuming observations, thus an electron analyzer or an integrating X-ray spectral detector can be utilized. Among the scanning microscopes, however, STXM combined with energy-resolved X-ray fluorescence detection (STXM-XRF) (for example, Kaulich *et al.*, 2011; Hitchcock *et al.*, 2012; Bozzini *et al.*, 2015; Lühl *et al.*, 2019) has high potentiality of simultaneous multi-element mapping for shortening long measurement time effectively.

Most of the existing spectromicroscopes have successfully been applied to surface science with high spatial resolution down to sub-100 nm. However, they have some inherent limitations. Since both TXM and STXM detect transmitted X-ray photons, a sample to be observed must be thin enough to enable the SX beam to transmit, which means they are not suitable for examining thick samples. Furthermore, since both SPEM and X-PEEM detect photoelectrons or secondary electrons, it is difficult to examine insulating materials without applying a metallic coating to avoid a surface charging effect.

Scanning SX spectromicroscopes using the photon-in/photon-out measurement scheme are able to overcome these limitations. Thus we have developed such a spectromicroscope to observe a thick sample under various environments. It is aimed at probing local electronic structures on the surfaces and interfaces of advanced materials, such as insulating bulk polymers, under conditions ranging from low vacuum to helium atmosphere. It can be easily applied to advancing the surface characterization of the membrane electrode assembly (MEA) of a working polymer electrolyte fuel cell (PEFC) (Litster & McLean, 2004; Zhang *et al.*, 2009), and it also enables us to observe wet samples including biological materials. These observations have generally not been feasible using conventional STXMs. Since target samples such as bulk polymer and biological materials are not radiation hardened against focused X-ray beams (Wang *et al.*, 2009*a*,*b*; Yamane *et al.*, 2019), the design must be optimized accordingly to ensure the following objectives are met: (i) investigating bulk polymer sample and biological materials in wet conditions under atmospheric pressure; (ii) avoiding X-ray damage during observation by employing quick-scan; (iii) accepting bulky sample holders, such as those for wet samples, by lengthening the working distance between the sample and the nearest optical element.

In this article, we describe in detail the designs and the current status of the present SX spectromicroscope. The present apparatus described here is able to realize the objectives mentioned above, at the expense of a modest spatial resolution of around 300–500 nm. The characteristics of the present spectromicroscope have been evaluated using the SX undulator radiation at BL17SU of SPring-8.

2. System description

Fig. 1 shows a schematic illustration and photographs of the apparatus installed at the b-branch of the SX undulator beamline, BL17SU (Ohashi *et al.*, 2006, 2007; Senba *et al.*, 2007; Oura *et al.*, 2007), at SPring-8. As shown in Fig. 1, the apparatus consists of three main components: the differential pumping chamber, the large rectangular chamber (hereafter referred to as the outer chamber) housing the microscope as

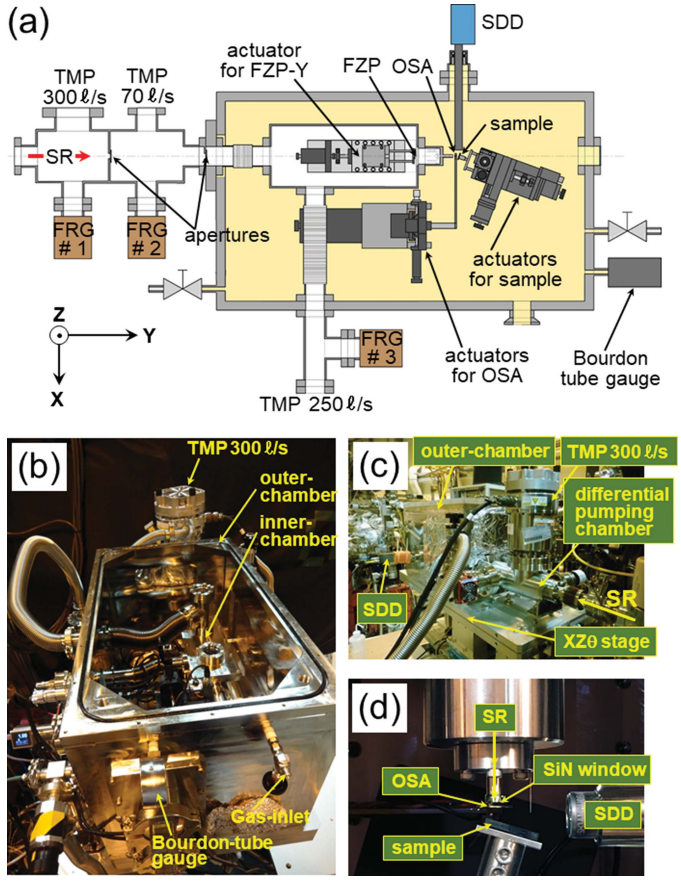

Figure 1
(*a*) Top-view schematic for the scanning soft X-ray spectromicroscope, where TMP is the turbo-molecular pump, FRG the full-range gauge, FZP the Fresnel zone plate, OSA the order-sorting aperture, SDD the silicon drift detector and SR the synchrotron radiation. (*b*, *c*, *d*) Photographs of the present apparatus: (*b*) the view from downstream, (*c*) the view from upstream, and (*d*) the area around the sample.

well as the sample actuators, and the $XZ\theta$-stage to align all components to the SX-beam axis. As shown in Fig. 1(*a*), the SX-beam direction is defined as the *Y*-axis, in the horizontal plane the *X*-axis is defined to be perpendicular to the SX beam, and the *Z*-axis is perpendicular to both the *X*- and *Y*-axes. The design concepts of the apparatus are described in detail in the following subsections.

2.1. Focusing optics

We utilized a Fresnel zone plate (FZP) as an optical component to focus the SX beam. The basic relationship between the focal length f_m in the mth order, the wavelength λ, the FZP radius r and the outermost zone width Δr can be expressed as (Attwood, 1999)

$$f_m = 2r\,\Delta r/(m\lambda). \tag{1}$$

To achieve a large working distance (~61 mm at 543 eV), we had to adjust the r and Δr parameters so that the product $2r \times \Delta r$ remained 139.23 μm^2. In the present configuration, the horizontal beam size at the sample position was measured to be about 940 μm full width at half-maximum (FWHM). Based on the beam size, we designed the FZP to have a fairly large 910 μm-diameter FZP patterned on a 1 mm × 1 mm silicon nitride (SiN) membrane (100 nm thick) supported by a Si substrate (10 mm × 10 mm × 0.2 mm-thick). The zone patterns were made of Au. The outermost zone width and the zone thickness were designed to be 153 nm and 190 nm (±15%), respectively. The FZP also had a 24 μm-diameter center beam stop fabricated by Applied Nanotools.

To sweep the energy of the SX beam, the FZP was firmly mounted on a vacuum-compatible motorized stage that moved 40 mm along the SX-beam axis (*i.e.* the FZP-*Y*-axis). The energy available for the SX beam covered by this actuator was designed to range from 400 to 756 eV for the first-order diffraction. The theoretical maximum efficiency for the first-order diffraction at 400 eV was calculated to be about 11%. The FZP and the FZP-*Y* actuator were housed in a small rectangular vacuum chamber (hereafter called the inner chamber) which had a thin SiN window (2 mm × 2 mm × 200 nm-thick) mounted at the end of the chamber to extract the focused SX beam from the inner chamber and project it onto the sample surface. The SiN window was used to isolate the inner chamber from the low-vacuum (several Pa at the lowest) or helium atmospheric conditions of the outer chamber for the sample area. An order-sorting aperture (OSA), a 25 μm pinhole, was placed between the SiN window and the sample. The OSA was used for selecting the first-order diffraction from the focused SX beam and was mounted on a motorized actuator to precisely align the OSA to the SX-beam axis.

The apparatus was installed downstream from the exit slit of the beamline monochromator so that the distance between the FZP and the exit slit, p, was about 11 m. The opening size of the exit slit was assumed to be the vertical size of the light source, σ_v, in the present focusing optics. As for the horizontal size of the light source, σ_h, we utilized settings of the fixed-width slit (*e.g.* 100, 50, 25 and 10 μm), which could be manually inserted into the photon-beam axis about 10 cm downstream from the exit-slit.

The theoretical spot size of the focused beam, δ_m, in the mth order can be expressed by the following equation (Yun *et al.*, 1999),

$$\begin{aligned}\delta_m &= \left(\delta_i^2 + \delta_g^2 + \delta_c^2\right)^{1/2} \\ &= \left[\left(\frac{1.22\Delta r}{m}\right)^2 + \left(\sigma\,\frac{q}{p}\right)^2 + \left(2r\,\frac{\Delta E}{E}\right)^2\right]^{1/2},\end{aligned} \tag{2}$$

where δ_i, δ_g and δ_c represent the diffraction-limited resolution, the geometrical resolution and the light monochromaticity, respectively. δ_i is obtained by applying the Rayleigh criterion and equals $1.22\Delta r/m$. δ_g depends on the source size, σ, the distance p between the FZP and the exit slit, and the distance q between the FZP and the sample. δ_c depends on the diameter $2r$ of the FZP and the energy resolution $\Delta E/E$ of the SX beam. By applying the parameters for the conditions of the present apparatus to equation (2), we expected to achieve a 223 (255) nm spot size of the focused beam for the 400 (720) eV SX beam, where the size of the light source and the corresponding energy resolution were assumed to be 20 μm and 10^{-4}, respectively.

2.2. Actuators

As shown in Fig. 1(*a*), the apparatus utilized three sets of motorized actuators in the outer chamber: (1) the vacuum-compatible motorized feedback-stage system for the FZP-*Y*-axis movement, (2) the *XYZ* actuators for positioning the OSA to the SX-beam axis, and (3) the *XZ* feedback-stage system, for two-dimensional sample scanning, mounted on the *Y*-axis actuator which is manually adjusted at the moment. Currently, the actuators for the OSA positioning and the sample scanning are not vacuum-compatible because they are often operated under helium atmospheric conditions. In the near future, however, they will be replaced with vacuum-compatible ones. The following subsections describe the details of the present actuators

2.2.1. Actuator for FZP. For the FZP-*Y*-axis movement, we employed a vacuum-compatible feedback-stage system [SIGMA TECH, FS-1040PX(V)] manufactured by SIGMA TECH Co. Ltd[1], which had an 80 mm-width × 60 mm-depth table-top and a 40 mm-long travel with ±20 nm repeatability. We carefully aligned the axis of the actuator's movement to that of the apparatus by using a well collimated HeNe laser beam (632.8 nm, 5 W) so as to maximize the straightness of the movement.

The FZP position frequently changed because its position had to be optimally adjusted according to the energy of the incident SX beam. So it was continuously adjusted when the apparatus was operated to record the SX absorption spectrum.

[1] The feedback-stage system used in the present apparatus was originally developed by SIGMA TECH Co. Ltd. SIGMA TECH transferred their business to SIGMAKOKI Co. Ltd on 1 June 2019; SIGMA TECH closed their business on 31 July 2019.

The maximum speed for the FZP-*Y*-axis movement was 2 mm s^{-1}, which will later be reduced to 0.5 mm s^{-1} for SX absorption spectroscopy, namely for micro-XAFS (X-ray absorption fine structure) mode.

2.2.2. Actuators for OSA positioning. We used 1 µm-resolution motorized *XZ* actuators, consisting of an actuator fitted with a compact stepping motor for each axis (SIGMAKOKI, SGSP-ACT). The *XZ* actuators, which have a ±3 mm movable range for each axis, were mounted on the manually adjustable *Y*-axis actuator and used for positioning the OSA to the SX beam axis. The diameter of the pinhole for the OSA was 25 µm, so that an accuracy of 1 µm was considered good enough for the *XZ* actuators of the OSA.

2.2.3. Actuators for sample scanning. To precisely scan samples for two-dimensional element-distribution and chemical-state mapping, piezo actuators are often used for sub-100 nm spatial resolution. In the present apparatus, to accommodate the large scanning area of the sample (up to a maximum of 20 mm × 20 mm), the *XZ* feedback-stage system (SIGMA TECH, FS-1020PXY), mounted on a manually adjustable *Y*-axis actuator, was employed for two-dimensional sample scanning. The present *XZ* actuators have a 60 mm-width × 60 mm-height table-top, with a 20 mm-long stroke for each axis, with ±20 nm repeatability. The maximum scanning speed was about 10 mm s^{-1} each. For measurements with SX-induced fluorescence mapping (*i.e.* the photon-in/photon-out measurement scheme), we employed the step-by-step scanning method, where the sample position was fixed for each measurement, for the element-distribution and chemical-state mapping. For the case of mapping with electron-yield measurements, we will be able to achieve a quick-scan by employing the so-called 'on-the-fly measurement scheme', in which the sample continuously moves during the measurements.

2.3. The vacuum system and the *XZθ* stage

As shown in Fig. 1(*a*), the vacuum system for the present apparatus can be separated into three parts: (1) the differential pumping chamber, (2) the inner chamber for the FZP optics, and (3) the outer chamber for the sample area. The following subsections describe the details of each part as well as the *XZθ* stage for the apparatus.

2.3.1. Differential pumping chamber. A two-stage differential pumping section at the most upstream part of the apparatus connected it to the SX beamline. This section is indispensable for safe operations when the inner chamber for the FZP optics is operated without the SiN window.

The first stage of the section consisted of a 70 l s^{-1} turbo-molecular pump (TMP) backed by a dry pump #2 (DP), and 2 mm-diameter and 1.5 mm-diameter apertures for the entrance- and exit-apertures, respectively. The pressure inside the first stage was monitored by a compact full-range gauge #2 (FRG, PFEIFFER PKR-261). Typical pressures during the experiment were about 7×10^{-6} Pa and about 8×10^{-4} Pa, respectively, for the conditions with and without the SiN window mounted at the end of the inner chamber.

The second stage of the section (*i.e.* the upstream side of the apparatus) similarly consisted of a 300 l s^{-1} TMP backed by a DP #1 and an FRG #1 for monitoring pressure. During the experiment, the pressure in the second stage was less than 2×10^{-6} Pa for both the conditions with and without the SiN window.

2.3.2. Inner chamber. The inner chamber was used for housing the FZP and the FZP-*Y* actuator, and was mainly evacuated by a 250 l s^{-1} TMP backed by a 70 l s^{-1} TMP and a DP #3. As mentioned above, the inner chamber usually had the thin SiN window mounted at the end of the inner chamber to extract the focused SX beam and project it onto the sample surface. The inner chamber could also operate without the thin SiN window. Typical pressures during the experiments were about 3×10^{-5} Pa and 4×10^{-3} Pa, respectively, for the conditions with and without the SiN window.

2.3.3. Outer chamber. The outer chamber housed the inner chamber, the OSA with the actuators, the actuators for sample scanning, and the detector for SX-induced fluorescence measurements. The outer chamber could be operated with either low vacuum (*e.g.* about 10 Pa) or helium atmospheric conditions. The outer chamber was evacuated by a DP #4 in the case of low-vacuum conditions. The pressure inside the outer chamber during the experiment was monitored using a Bourdon-tube gauge (DAIICHI KEIKI SEISAKUSYO Co. Ltd) and an active sensor (Leybold, PENNINGVAC PTR90N).

2.3.4. The *XZθ* stage. All vacuum chambers were seated on a θ-adjustable table that was firmly supported by an *XZ* stage to align the apparatus to the SX beam. The *XZ* supporting stage movements were monitored precisely by Mitutoyo digimatic indicators (ID-C112, repeatability <0.002 mm). The *XZ* supporting stage was levelled to be on a precise horizontal plane using the adjuster legs. The rotation center of the θ-adjustable table was on the focal point for the FZP optics. θ was carefully adjusted to align the FZP-*Y*-axis movement with the axis of the SX beam.

2.4. Detector

As shown in Fig. 1(*a*), we mainly utilized a solid-state silicon drift detector (SDD) (Amptek XR-100FASTSDD), which was thermoelectrically cooled, to achieve the photon-in/photon-out measurement scheme. The present SDD, which had a 500 µm-thick 25 mm^2 active area, included a silicon nitride window with an aluminium coating (Patented 'C-series' X-ray windows) to extend the low-energy response down to boron. The SDD could provide a resolution of 126 eV FWHM at the Mn $K\alpha$ line. The output of the SDD's preamplifier was fed into a high-performance digital pulse processor (Amptek PX5) to digitize the signal for generating an energy spectrum of SX-induced fluorescence from the sample surface.

DPPMCA (Windows software from Amptek) was used for data acquisition, display and control for the Amptek signal processors. We were able to apply several regions of interest (ROI) on the fluorescence spectrum, and the PX5 provided up to eight outputs of a single channel analyzer (SCA) to record

the element-specific SX absorption spectrum by partial fluorescence yield spectroscopy. When we tuned the energy of the incident SX beam to that of the resonance energy for the site-specific chemical state, we were able to use the output from the SCA to produce chemical-state mapping for the sample surface.

We are also developing a configuration to acquire element-specific information by collecting the photoelectrons as well as the secondary electrons emitted from the sample surface by using a biased OSA connected to a picoammeter. The back-plane of the OSA, which faces the sample surface, is coated with vacuum evaporated Au. The output from the picoammeter is directly read via the GPIB interface.

For bulk-sensitive SX-induced fluorescence measurements, it is necessary to acquire the signals using the pulse-counting mode because of the low counting efficiency due to low fluorescence yields of the light elements. For surface-sensitive electron yield measurements, we expect a large number of secondary electrons to be emitted because the inner-shell vacancies of the light elements are going to mostly decay through Auger electron emission, causing cascading secondary electron emissions due to inelastic scattering. Thus, we expect high-speed data acquisition by measuring the photocurrent using the picoammeter, which can potentially enable us to carry out quick-scans. We are now exploring efficient schemes for electron collection using the OSA.

2.5. Software

Control of both the actuator as well as data acquisition is carried out using LabVIEW (NI) based software applications. The following are some examples of software applications we have provided for the present spectromicroscope:

(i) One-dimensional (either *X*- or *Z*-axis) and two-dimensional (*X*- and *Z*-axes) OSA positioning applications.

(ii) Application for *X*- and *Z*-axes scan of the knife-edge to measure the spot size of the focused SX beam.

(iii) Application for FZP-*Y*-axis movement to survey the best focusing conditions.

(iv) One-dimensional (either *X*- or *Z*-axis) and two-dimensional (*X*- and *Z*-axes) sample scanning application to measure element-specific and chemical-state-specific mapping.

(v) Application for micro-XAFS combined with sample-position changing as well as helicity switching capabilities.

We plan to modify these software applications and develop new applications based on user demand.

3. Alignment and adjustment of the apparatus

Before characterizing the apparatus using SX undulator radiation, we carefully aligned all the small apertures installed in the differential pumping chamber, the actuator's axis for the FZP-*Y*-axis movement, and the center of the SiN window mounted at the end of the inner chamber. We utilized a theodolite and a well collimated HeNe laser beam for the precise pre-alignment of these components.

The apparatus was installed at the carry-in station, where two end-stations could be easily switched by using the slide-rails, of the b-branch of beamline BL17SU. In this carry-in station, the present apparatus or the versatile PEEM machine (FOCUS PEEM, FOCUS GmbH) (Ohkochi *et al.*, 2019) could be alternatively installed. We had to carry out the following alignment and adjustment procedures for the present apparatus each time after switching the end-station.

3.1. Alignment of the apparatus

As a first step, we aligned the apparatus axis to that of the SX undulator radiation by adjusting the *XZ* supporting stage of the apparatus as well as the θ adjustment capability to maximize the transmitted SX-beam intensity by monitoring the output of the photodiode (AXUV-20HE1, IRD Inc.) mounted downstream of the SiN window at the inner chamber.

3.2. Positioning the OSA

After aligning the apparatus, the position of the FZP-*Y*-axis was temporarily set to a calculated rough position to achieve a focused SX beam a few micrometres in size. Then, using this SX beam, the position of the OSA was two-dimensionally scanned while monitoring the transmitted SX-beam intensity using the photodiode. When we recognized the SX-beam spot on the two-dimensional map as shown in Fig. 2(*a*), we carried out several one-dimensional scans for the *X*- and *Z*-axes to finely optimize the *X*- and *Z*-axis positions of the OSA as shown in Figs. 2(*b*) and 2(*c*).

3.3. Adjustment of the FZP-*Y*-axis

As mentioned above, the FZP-*Y*-axis position had to be adjusted to satisfy the focusing conditions for a specific SX-energy. Therefore, to obtain the optimal focusing for the SX beam, we carried out measurements to make a correlation map between the FZP-*Y*-axis position and the SX-beam intensity profile by scanning the knife-edge for both the *X*-axis and the *Z*-axis. The focused beam size was obtained by differentiating the profile. For this purpose, we used the *XZ* actuators for sample scanning to scan the knife-edge. Fig. 3(*b*) shows a typical example of the correlation map measured for determining the FZP-*Y*-axis position to give the best focusing condition in the vertical direction. The incident SX-beam energy was 600 eV and the vertical source size was roughly 50 µm (*i.e.* the opening size of the exit-slit of the beamline optics). The constricted shape of the correlation map in Fig. 3(*b*) provided the best focusing FZP-*Y*-axis position as shown in Fig. 3(*c*). The resultant focused size was estimated to be about 777 nm FWHM by differentiating the intensity profile measured by the *Z*-axis scan of the knife-edge as shown in Fig. 3(*a*). The width was determined by the least-squares fitting procedure by employing a Gaussian function.

By applying the experimental conditions of the feasibility study for Fig. 3 to equation (2), we obtained a theoretical value for δ_m of 383 nm, where the diffraction-limited resolution δ_i = 187 nm, the geometrical resolution δ_g = 308 nm and

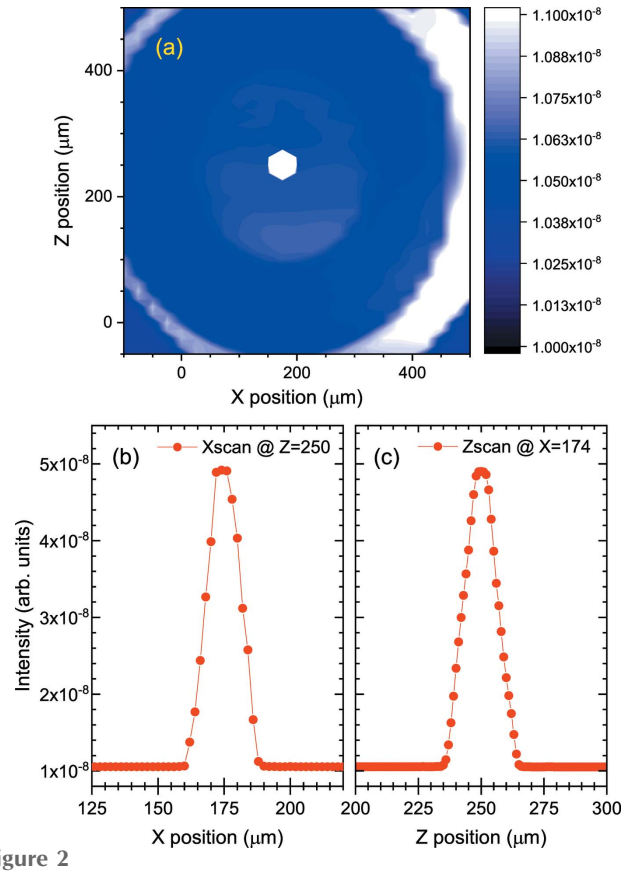

Figure 2
(*a*) Two-dimensional map of the transmitted SX-beam intensity by scanning the OSA *XZ*-positions recorded using the photodiode downstream of the SiN window. (*b*, *c*) One-dimensional scan profiles of *X*- and *Z*-axes of the OSA.

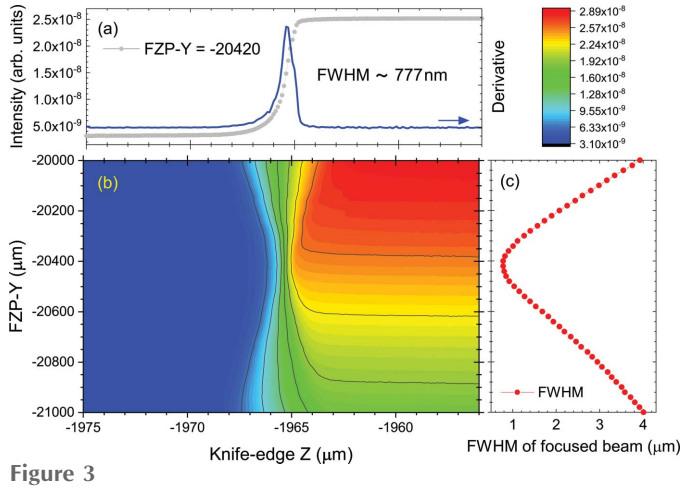

Figure 3
(*a*) Intensity profile measured by scanning the knife-edge for the *Z*-axis and its derivative showing the width of the focused SX beam at the FZP-*Y*-axis position of −20420 μm. (*b*) Correlation map between the FZP-*Y*-axis position and the SX-beam profile. (*c*) Deduced FWHM of the SX-beam profile as a function of the FZP-*Y*-axis position.

the light monochromaticity term δ_c = 130 nm for $E/\Delta E \simeq$ 7000. We found that the focused beam size measured nearly twice the theoretical value in the present feasibility study. To date, we have achieved a focused SX beam of 309 nm FWHM as the best focusing for conditions of the excitation energy E of 725 eV and the vertical source size σ_v of 20 μm. This value is a little larger than the theoretical value for δ_m of 255 nm under an energy resolution $\Delta E/E$ of 10^{-4}.

Possible reasons for the present focused SX-beam size being larger than the one calculated include mechanical vibration around the apparatus, error in the alignment accuracy of the focusing optical components, error in the determination of the exact focusing point of the FZP-*Y*-axis position, and tilt (Chao *et al.*, 2009) or distortion of the FZP itself. Regarding mechanical vibration around the apparatus, we attempted to stop all probable sources of vibration around the apparatus (*e.g.* the vacuum pumps near the apparatus), but were unable to improve the resolution. As for errors in the alignment accuracy and determination of the focusing point, we carefully adjusted the apparatus, but did not see any significant improvements. The tilt and distortion of the FZP itself may be the most likely cause, because the present FZP has a fairly large diameter (910 μm), making it susceptible to distortion, like a concave shape. This cause seems to be supported by the fact that there have been a few accidental breakdowns of the SiN window of the inner chamber, which has resulted in serious damage to the FZP (rupture of the FZP due to an inrush of air). The FZP is always exposed to harsh conditions, especially when the apparatus is operated without the SiN window mounted at the end of the inner chamber. We are now trying to find a solution to improve spatial resolution, but in parallel we would like to start experimental applications for the present spectromicroscope for several projects with modest (300–500 nm) spatial resolution.

3.4. Photon flux at the sample position

We have measured and estimated the relative photon intensities of the focused SX beam under conditions of low-vacuum and atmospheric pressure at the sample position. We have used a photodiode mounted at 3.1 mm, *i.e.* the focal point, from the SiN window. As a typical example, we optimized the focusing optics for E = 600 eV and σ_v = 100 μm.

In the case of low-vacuum conditions ($P_{outer} \simeq$ 10 Pa) in the outer chamber, the photon intensity was measured to be 40 nA of the photodiode output. This value corresponds to a photon flux of 1.5 × 10^9 photons s^{-1} and is defined as I_{Vac}. When we introduced air into the outer chamber to achieve atmospheric pressure, the resultant photon flux I_{Air} was measured to be decreased to 1 × 10^7 photons s^{-1}. This result indicated that the reduction factor R_{Air}, I_{Air}/I_{Vac}, was 6.7 × 10^{-3}, where the measured R_{Air} was in good agreement with the calculated value of 6.63 × 10^{-3} (CXRO, 2019). The photon flux under atmospheric pressure I_{Air} was calculated based on the Beer–Lambert law. The photoabsorption cross section μ_i of each nitrogen, oxygen, carbon and argon atom at 600 eV was deduced by interpolating the tabulated photoabsorption cross sections (Henke *et al.*, 1993). The total photoabsorption cross section μ of air was simply calculated as $\mu = \sum_i f_i \mu_i$ (i = N_2, O_2, CO_2, Ar), where f_i is the fraction of each component in air. These fractions as well as the density for the standard atmosphere were taken from Chronological

Scientific Tables (Rikanenpyo). By adapting the path-length of air, *i.e.* 3.1 mm in the present case, we could calculate I_{Air}/I_{Vac} to be 6.88×10^{-3} and confirm that the theoretical R_{Air} was in good agreement with the measured R_{Air}.

On the other hand, when we introduced helium into the outer chamber while monitoring the oxygen concentration meter, the photon flux was measured to be about 1.48×10^{9} photons s^{-1}. The corresponding reduction factor R_{He}, I_{He}/I_{Vac}, was estimated to be about 0.987 relative to the low-vacuum conditions, which is very close to our expected value, ~1. Under the above conditions for helium atmosphere, we confirmed that the counting rate of oxygen $K\alpha$ X-ray emission, excited by a 720 eV focused SX-beam, from the glass plate, was about 1600 to 1700 counts s^{-1}.

4. Feasibility studies

We carried out several feasibility studies for the apparatus, such as element distribution mapping, XAFS for micro-sized areas, electron collection by the OSA, and observation of magnetic domain structures. All measurements for these feasibility studies were carried out under low-vacuum conditions in the outer chamber. The following subsections present typical results from the feasibility studies.

4.1. Element distribution mapping

In Fig. 4, we show the results of the demonstration for element distribution mapping. We utilized the patterned sample shown in Fig. 4(*a*). The patterned sample had a number of micro-dots made of permalloy ($Ni_{81}Fe_{19}$) fabricated on the silicon substrate. It was kept exposed to air for a long time, so it may have a naturally grown oxide layer on its surface. The largest circular-shaped pattern had a diameter of about 30 µm. The patterned sample was mounted onto the *XZ* actuators for sample scanning. The incident angle of the focused SX beam onto the sample was about 80°, which was close to the normal incidence, for enabling the SDD to measure SX-induced fluorescence from the sample surface. We adjusted the sample position to irradiate the focused SX beam of 780 eV onto the silicon layer and the permalloy layer and recorded the fluorescence spectra from each sample position, as shown in Fig. 4(*b*).

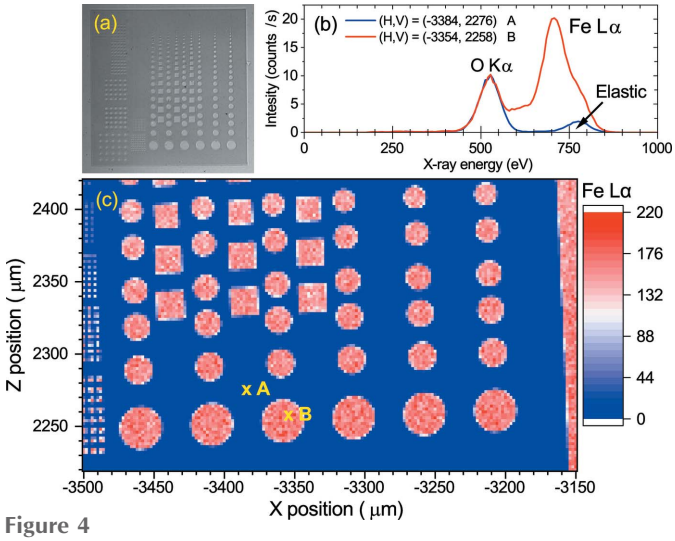

Figure 4
(*a*) Photograph of the patterned sample, taken using a metallurgical microscope. The micro-dot patterns made of permalloy ($Ni_{81}Fe_{19}$) were fabricated on the silicon substrate. (*b*) The SX-induced fluorescence spectra recorded inside the micro-dot (red-curve, point B) and outside the micro-dot (blue-curve, point A). (*c*) Element-specific two-dimensional mapping measured by counting the number of Fe $L\alpha$ X-rays.

We set a ROI on the fluorescence spectrum for the SCA output (the energy region of Fe $L\alpha$ X-rays) for the element-specific two-dimensional mapping. As can be seen in Fig. 4(*b*), however, we have to pay attention to the fact that the ROI set for the Fe $L\alpha$ X-rays included a definite fraction of elastic scattering component. In this feasibility measurement, we operated the insertion device ID17 of BL17SU (Oura *et al.*, 2007; Shirasawa *et al.*, 2004) in helical undulator mode and estimated the contribution of the elastic scattering to be about 25%. We can reduce the contribution of elastic scattering when we operate the ID17 to be the horizontally polarized linear undulator mode for the present setting. We counted the number of the SCA outputs by scanning the *XZ* actuators, and the resultant mapping is shown in Fig. 4(*c*) with pixel size of 2 µm. The dwell time per pixel was 1 s for the element distribution mapping. The observed image exhibited the expected pattern and the smallest pattern was resolved, as shown in the left-upper corner of Fig. 4(*c*).

4.2. XAFS for micro-sized areas

To demonstrate micro-XAFS capabilities, we carried out measurements of the SX absorption spectra inside and outside the micro-dot of the patterned sample. First, we performed two-dimensional sample scanning [*i.e.* 70 µm (H) × 40 µm (V) with 1 µm step] using a 760 eV SX beam (FWHM ≃ 550 nm) to determine the positions for the micro-XAFS measurements, as shown in Fig. 5(*a*). The pattern size of the square was about 20 µm × 20 µm. The typical measurement time for Fig. 5(*a*) was about 80 min. We set a ROI for the SCA output to be in the Fe $L\alpha$ X-ray region, similar to the case in the previous subsection. In Fig. 5(*a*), the red parts exhibit a higher counting rate, indicating that the red and blue parts are associated with the permalloy and the silicon substrate, respectively. We recorded the SX absorption spectra using partial fluorescence yield spectroscopy inside and outside the micro-sized area by sweeping the SX-beam energy around the $L_{2,3}$-edges and changing the position of the sample as shown in Fig. 5(*b*). We spent about 24 min recording these two spectra. The change in the spectral shape is recognizable across the boundary of the area.

The micro-XAFS provided information about the local electronic structure on the sample surface. When we tuned the energy of the SX beam to the specific structure observed in the micro-XAFS spectrum, it was possible to visualize the specific chemical-state distribution on the sample surface by means of chemical-state mapping.

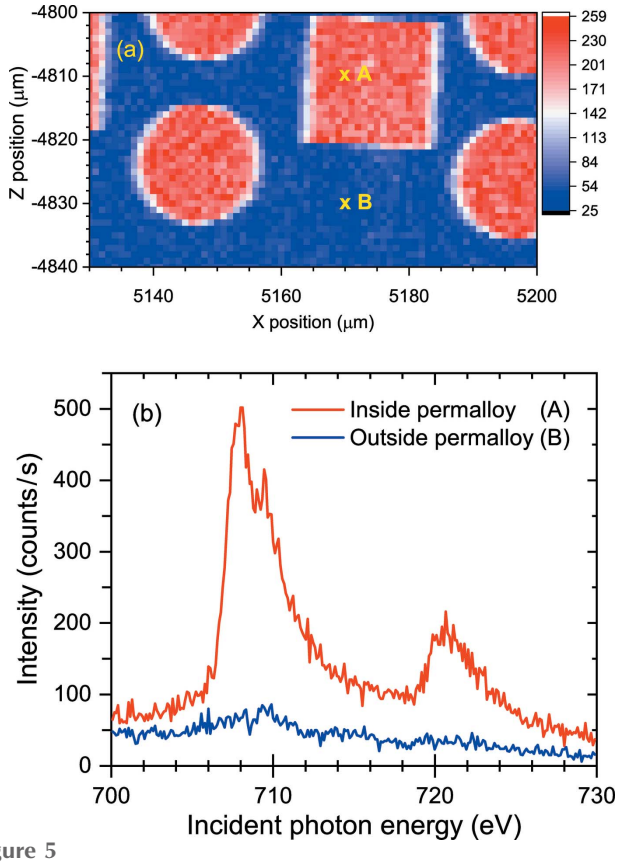

Figure 5
(*a*) Element-specific two-dimensional mapping measured using a 760 eV SX beam. (*b*) Micro-XAFS recorded inside the micro-dot (red-curve, point A) and outside the micro-dot (blue-curve, point B) by sweeping the SX-beam energy around the Fe $L_{2,3}$-edges.

4.3. Electron collection by OSA

We tried to collect the electrons using a biased OSA connected to a picoammeter to achieve high-speed data acquisition by measuring photocurrents due to secondary electron emissions. For the feasibility study, we used the *Z*-axis knife-edge as a photo-emitter and measured the photocurrent during the knife-edge scan. Fig. 6 shows the results of the measured profiles. The line with blue open-circles shows the profile of the SX beam measured using a photodiode. The line with red filled-circles indicates the photocurrent intensity profile measured along the *Z*-axis of the knife-edge surface. The energy of the SX beam was 720 eV, near (above) the Fe L_2 (L_3) edge. The positions of the edge-jumps coincide with each other. The edge-jump for the photocurrent was about 7 pA, comparable with the total electron yield current of the order of 10 pA measured using a scanning SX microscope recently developed at beamline BL25SU at SPring-8 for magnetic imaging (Kotani *et al.*, 2018). Since the line shape of the measured photocurrent was rather noisy, we are pursuing further improvements to electron collection.

A possible solution to realize the high-speed data acquisition with high-efficiency electron-yield measurement is to utilize an electron multiplier. As Watts &McNeill (2010) have succeeded in performing simultaneous surface and bulk

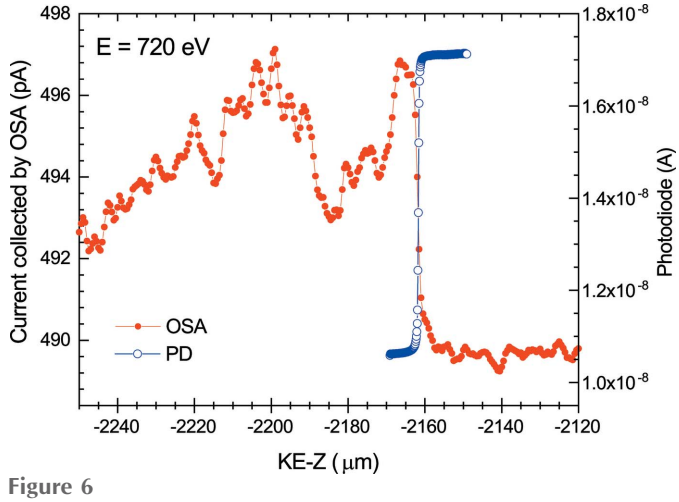

Figure 6
Results from the feasibility study for electron collection using the OSA. The line with blue open-circles indicates the profile of the 720 eV SX beam measured by scanning the knife-edge for the *Z*-axis using a photodiode. The line with red filled-circles shows the profile of the photocurrent intensity measured along the *Z*-axis of the surface of the knife-edge.

imaging of polymer blend film by setting the channeltron and photomultipier tube for their STXM, we are also designing a detection system for the electron-yield measurement using a large solid-angle electron multiplier.

4.4. Observation of magnetic domain structures

For the feasibility study to observe magnetic domain structures, we utilized the same permalloy/silicon patterned sample. We tuned the SX-beam energy to 708 eV to selectively excite an electron in the L_3-subshell to an unoccupied state of Fe, and counted the number of resonant SX emissions by changing the *XZ* position of the sample. Fig. 7 shows the results of the element-specific two-dimensional mapping for the permalloy pattern. The diameter of the pattern was about 20 μm and the step-size for the mapping measurement (*i.e.* the pixel size) was 1 μm for both the *X*-axis and the *Z*-axis. The typical measurement time for this mapping was about 20 min for each helicity. To observe the Fe magnetic domain structure, we switched the helicity of the incident SX beam by controlling ID17 in the helical undulator mode. As shown in Figs. 7(*a*) and 7(*b*), the domain structure reversed corresponding to the helicity of the circularly polarized SX beam. As the permalloy is a ferromagnetic material, the red-part observed in Fig. 7 shows the magnetization parallel to the helicity of the incoming SX beam. When we scanned the sample position with a much finer step-size, it was possible to observe a much clearer magnetic domain structure.

5. X-ray absorbed dose for the typical XRF experiment

As we have mentioned previously, investigations of bulk polymer as well as biological materials, which are not radiation hardened against a focused X-ray beam (Wang *et al.*, 2009*a*,*b*; Yamane *et al.*, 2019), are involved in our objectives so that we

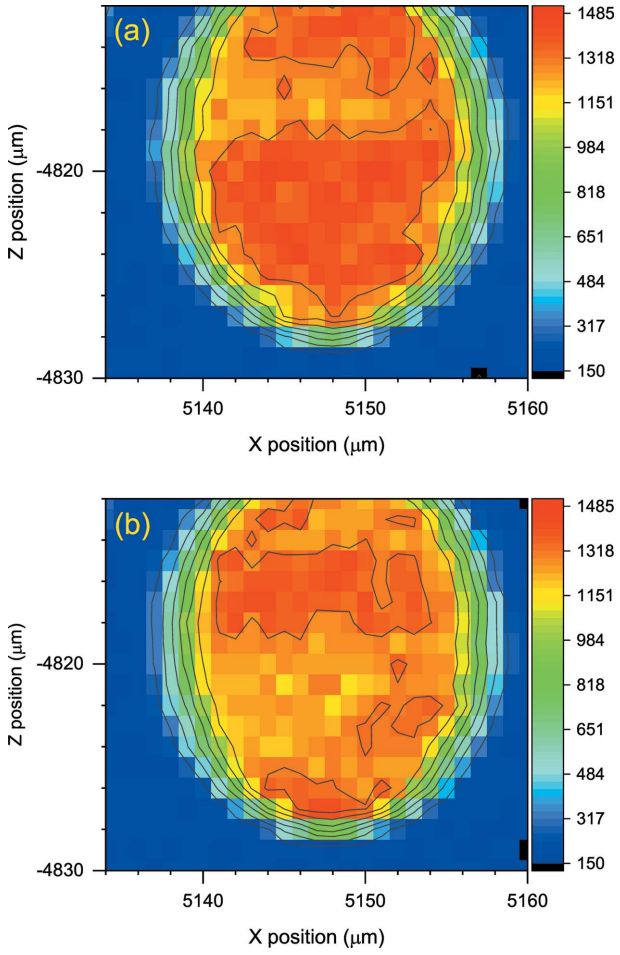

Figure 7
The element-specific two-dimensional mapping measured by counting the number of Fe $L\alpha$ X-rays at the L_3-edge maximum. The Fe magnetic domain structure was observed to be reversed, corresponding to the helicity of the circularly polarized SX beam. (*a*) For left circular polarization and (*b*) for right circular polarization.

need to estimate the X-ray absorbed dose for the XRF measurements on such materials.

Here we bring up Nafion®, which is often used as an electrolyte material in PEFC, as a typical example for estimating the X-ray absorbed dose. We have employed the chemical structure of Nafion 117 (Ghassemzadeh *et al.*, 2010) in the sulfonic acid form (Fig. 8) to evaluate the photoabsorption cross sections near the *K*-edge of fluorine. Characteristics of Nafion 117 are summarized in Table 1.

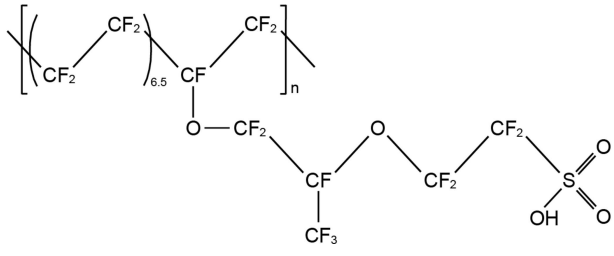

Figure 8
Chemical structure of Nafion 117.

Table 1
Characteristics of Nafion 117.

Molecular unit	$C_{20}H_1O_5F_{39}S_1$	
Atomic % of different elements	Cabon 30.3%, hydrogen 1.5%, oxygen 7.6%, fluorine 59.1%, sulfur 1.5%	
Density, ρ (g cm^{-3})	1.98†	
Photoabsorption cross section, $\mu(E_x)$ (cm^2 g^{-1})	Calculation‡	Experiment§
μ(676.8)	3000	–
μ(685)	2916	∼4380
μ(690)	–	∼23 540
μ(705)	11 320	∼12 830
Transmission, $T(E_x)$ [$= I/I_0 = \exp(-\mu\rho t)$]	Calculation‡	Experiment§
T(676.8)	0.9707¶	–
T(685)	0.9715¶	0.9576¶
T(690)	–	0.7921¶
T(705)	0.8940¶	0.8807¶
Incident X-rays attenuation length (nm) at 690 eV, $t_{1/e}$ ($t_{1/10}$)	211 (486)	
Effective probing depth (nm) at F $K\alpha$ X-ray energy, $d_{1/e}$ ($d_{1/10}$)	125 (285)	

† Sigma-Aldrich; see, for example, https://www.sigmaaldrich.com/content/dam/sigma-aldrich/docs/SAJ/Brochure/1/j_nafion_recipe.pdf (in Japanese). ‡ Calculated based on the Beer–Lambert law. § Evaluated from the measured optical density (Martens *et al.*, 2019). ¶ A 50 nm layer thickness was assumed.

Firstly, we estimated the photoabsorption cross sections below the *K*-edge (685 eV), 1*s* peak (690 eV) and above the *K*-edge (705 eV) of fluorine. Similar to the case described in Section 3.4, we deduced the corresponding values using the tabulated photoabsorption cross sections (Henke *et al.*, 1993) for the elements contained in Nafion 117, and then we obtained the photoabsorption cross section $\mu^{\rm Calc.}_{\rm Nafion}$ at 685 eV (705 eV) as 2916 cm^2 g^{-1} (11320 cm^2 g^{-1}) accordingly. By referring the measured optical density of perfluorosulfonic acid (PFSA) at the F 1*s* peak at 690 eV (Martens *et al.*, 2019), we could estimate the photoabsorption cross section $\mu^{\rm Exp.}_{\rm Nafion}$ at 690 eV to be about 23540 cm^2 g^{-1}. By using these photoabsorption cross sections and the density of Nafion 117, we calculated the transmission $T(E_x)$ for each excitation energy as shown in Table 1.

Secondly, we estimated the incident X-rays attenuation length $t_{1/e}$ ($t_{1/10}$), where the intensity of X-rays decreases to 1/e (1/10) of its primary value at the sample surface, and the effective probing depth of the fluorescence spectrum $d_{1/e}$ ($d_{1/10}$). By using the photoabsorption cross section of Nafion 117, we determined $t_{1/e}$ ($t_{1/10}$) to be 211 nm (486 nm) for the F 1*s* resonant excitation. In the present setup, since the incidence angle of the focused SX beam onto the sample surface was about 80° and the SDD for the SX-induced fluorescence measurement was mounted to be perpendicular to the SX-beam axis, we needed to pay attention to the fact that the detectable fluorescence signals from the layer deep inside the bulk of sample were severely affected by the self-absorption for the F $K\alpha$ X-rays due to the sample itself. The resultant depth contributing to the measured fluorescence spectrum was estimated at the F $K\alpha$ energy, *i.e.* 676.8 eV, to be $d_{1/e}$ ($d_{1/10}$) $\simeq$ 125 nm (285 nm) from the sample surface. Thus we only

considered the near surface layer, *e.g.* ∼50 nm, for estimating the X-ray absorbed dose.

Finally, we evaluated the X-ray absorbed dose for the stack of 50 nm-thick layers of Nafion 117. As reported by Yamane *et al.* (2019), we estimated the absorbed dose rate for the first 50 nm-thick layer of the stack to be about 1560 MGy s^{-1}. As Martens *et al.* (2019) have pointed out, PFSA is very sensitive to X-ray exposure and results in changes to their physical morphology and chemistry even at low nominal dose (5–6 MGy). Thus, if we set the critical absorbed dose for Nafion 117 to be 5 MGy, we need to measure the sample surface for chemical state mapping by quick-scan, *i.e.* about 3.2 ms for one pixel (∼500 nm), before the sample is severely damaged. In order to realize such high-speed chemical state mapping with a reasonable signal-intensity, it is indispensable to implement a large solid-angle SDD system, as in the case of the four-channel SDD system reported by Lühl *et al.* (2019), for the investigations of bulk polymer and biological materials. In the case of the measurements on electrically conductive materials, on the other hand, we will be able to apply a high-efficiency electron-yield measurement system employing a large solid-angle electron multiplier, which is under development for quick-scan. For the former materials, until the implementation of such large solid-angle multi-element SDD system is realized, we need to reduce the incident photon flux density by defocusing the SX beam to 1 or little larger micrometre spot-size at the sample surface giving rise to saving a factor of four or more in the absorbed dose. Even though such a quick-scan system is realized, we have to keep in mind the fact that severe damage of the sample will be inevitable after the micro-XAFS measurement across the absorption edge.

6. Summary

In summary, we have developed a scanning SX spectro-microscope based mainly on the photon-in/photon-out measurement scheme to probe local electronic structures on the surfaces and interfaces of advanced materials under conditions ranging from low-vacuum to helium atmosphere. We demonstrated the performance of the spectromicroscope by observing the permalloy micro-dot patterns fabricated on a silicon substrate using a focused SX beam with a modest spatial resolution (*e.g.* ∼500 nm). We evaluated the X-ray radiation dose for Nafion® at the fluorine *K*-edge as a typical example of material, which is not radiation hardened against a focused SX beam, for near-future experiments.

Acknowledgements

The synchrotron radiation experiments were performed at beamline BL17SU at SPring-8 with the approval of the RIKEN SPring-8 Center (proposal Nos. 20180001, 20180058, 20190040 and 20190045). MO would like to thank Dr Tetsuya Nakamura of JASRI (present address: Tohoku University/PhoSIC) for providing his long-focal-length FZP for our experiments during the early stage of this project. The authors are grateful to Dr Takuo Ohkochi of JASRI and Professor Akinobu Yamaguchi of the University of Hyogo for providing a patterned sample used in the present study. HY would like to thank Dr Takuji Ohigashi of UVSOR of the Institute for Molecular Science for his valuable advice for the helium-path condition. The authors would also like to thank the members of the Engineering Team of the RIKEN SPring-8 Center for their technical assistance.

Funding information

Funding for this research was provided by: JST-Mirai Program (grant No. JPMJMI18A2).

References

Abyaneh, M. K., Gregoratti, L., Amati, M., Dalmiglio, M. & Kiskinova, M. (2011). *e-J. Surf. Sci. Nanotech.* **9**, 158–162.
Attwood, D. (1999). *Soft X-rays and Extreme Ultraviolet Radiation: Principles and Applications*, pp. 337–394. Cambridge University Press.
Bozzini, B., Bocchetta, P., Alemán, B., Amati, M., Gianoncelli, A., Gregoratti, L., Sezen, H., Taurino, A. & Kiskinova, M. (2015). *J. Mater. Chem. A*, **3**, 19155–19167.
Chao, F.-H., Yin, G.-C., Liang, K. S. & Lai, Y.-C. (2009). *Proc. SPIE*, **7448**, 74480X.
CXRO (2019). *X-ray Database of the Center for X-ray Optics: X-ray Interactions With Matter*, http://henke.lbl.gov/optical_constants/gastrn2.html.
Ghassemzadeh, L., Kreuer, K.-D., Maier, J. & Müller, K. (2010). *J. Phys. Chem. C*, **114**, 14635–14645.
Günther, S., Kaulich, B., Gregoratti, L. & Kiskinova, M. (2002). *Prog. Surf. Sci.* **70**, 187–260.
Guttmann, P. & Bittencourt, C. (2015). *Beilstein J. Nanotechnol.* **6**, 595–604.
Henke, B. L., Gullikson, E. M. & Davis, J. C. (1993). *At. Data Nucl. Data Tables*, **54**, 181–342.
Hitchcock, A. P., Obst, M., Wang, J., Lu, Y. S. & Tyliszczak, T. (2012). *Environ. Sci. Technol.* **46**, 2821–2829.
Horiba, K., Nakamura, Y., Nagamura, N., Toyoda, S., Kumigashira, H., Oshima, M., Amemiya, Y., Senba, Y. & Ohashi, H. (2011). *Rev. Sci. Instrum.* **82**, 113701.
Kaulich, B., Thibault, P., Gianoncelli, A. & Kiskinova, M. (2011). *J. Phys. Condens. Matter*, **23**, 083002.
Kotani, Y., Senba, Y., Toyoki, K., Billington, D., Okazaki, H., Yasui, A., Ueno, W., Ohashi, H., Hirosawa, S., Shiratsuchi, Y. & Nakamura, T. (2018). *J. Synchrotron Rad.* **25**, 1444–1449.
Leontowich, A. F. G., Berg, R., Regier, C. N., Taylor, D. M., Wang, J., Beauregard, D., Geilhufe, J., Swirsky, J., Wu, J., Karunakaran, C., Hitchcock, A. P. & Urquhart, S. G. (2018). *Rev. Sci. Instrum.* **89**, 093704.
Leung, B. O., Brash, J. L. & Hitchcock, A. P. (2010). *Materials*, **3**, 3911–3938.
Litster, S. & McLean, G. (2004). *J. Power Sources*, **130**, 61–76.
Lühl, L., Andrianov, K., Dierks, H., Haidl, A., Dehlinger, A., Heine, M., Heeren, J., Nisius, T., Wilhein, T. & Kanngießer, B. (2019). *J. Synchrotron Rad.* **26**, 430–438.
Martens, I., Melo, L. G. A., Wilkinson, D. P., Bizzotto, D. & Hitchcock, A. P. (2019). *J. Phys. Chem. C*, **123**, 16023–16033.
Ohashi, H., Senba, Y., Ishiguro, E., Goto, S., Shin, S. & Ishikawa, T. (2006). *Proc. SPIE*, **6317**, 63171A.
Ohashi, H., Senba, Y., Kishimoto, H., Miura, T., Ishiguro, E., Takeuchi, T., Oura, M., Shirasawa, K., Tanaka, T., Takeuchi, M., Takeshita, K., Goto, S., Takahashi, S., Aoyagi, H., Sano, M., Furukawa, Y., Ohata, T., Matsushita, T., Ishizawa, Y., Taniguchi, S., Asano, Y., Harada, Y., Tokushima, T., Horiba, K., Kitamura, H., Ishikawa, T. & Shin, S. (2007). *AIP Conf. Proc.* **879**, 523–526.

Ohigashi, T., Ito, A., Shinohara, K., Tone, S., Kado, M., Inagaki, Y., Wang, Y.-F. & Kosugi, N. (2016). *AIP Conf. Proc.* **1696**, 020027.
Ohkochi, T., Osawa, H., Yamaguchi, A., Fujiwara, H. & Oura, M. (2019). *Jpn. J. Appl. Phys.* **58**, 118001.
Oura, M., Nakamura, T., Takeuchi, T., Senba, Y., Ohashi, H., Shirasawa, K., Tanaka, T., Takeuchi, M., Furukawa, Y., Hirono, T., Ohata, T., Kitamura, H. & Shin, S. (2007). *J. Synchrotron Rad.* **14**, 483–486.
Prabu, V., Obst, M., Hosseinkhannazer, H., Reynolds, M., Rosendahl, S., Wang, J. & Hitchcock, A. P. (2018). *Rev. Sci. Instrum.* **89**, 063702.
Schofield, P. F., Smith, A. D., Scholl, A., Doran, A., Covey-Crump, S. J., Young, A. T. & Ohldag, H. (2014). *Coord. Chem. Rev.* **277–278**, 31–43.
Senba, Y., Ohashi, H., Kishimoto, H., Miura, T., Goto, S., Shin, S., Shintake, T. & Ishikawa, T. (2007). *AIP Conf. Proc.* **879**, 718–721.
Shirasawa, K., Tanaka, T. Seike, T. Hiraya, A. & Kitamura, H. (2004). *AIP Conf. Proc.* **705**, 203–206.
Wang, J., Botton, G. A., West, M. M. & Hitchcock, A. P. (2009*b*). *J. Phys. Chem. B*, **113**, 1869–1876.
Wang, J., Morin, C., Li, L., Hitchcock, A. P., Scholl, A. & Doran, A. (2009*a*). *J. Electron Spectrosc. Relat. Phenom.* **170**, 25–36.
Watts, B. & McNeill, C. R. (2010). *Macromol. Rapid Commun.* **31**, 1706–1712.
Yamane, H., Oura, M., Sawada, K., Ebisu, T., Ishikawa, T., Yamazaki, N., Hasegawa, K., Takagi, K. & Hatsui, T. (2019). *J. Electron Spectrosc. Relat. Phenom.* **232**, 11–15.
Yun, W., Lai, B., Cai, Z., Maser, J., Legnini, D., Gluskin, E., Chen, Z., Krasnoperova, A. A., Vladimirsky, Y., Cerrina, F., Di Fabrizio, E. & Gentili, M. (1999). *Rev. Sci. Instrum.* **70**, 2238–2241.
Zhang, S. S., Yuan, X. Z., Wang, H. J., Merida, W., Zhu, H., Shen, J., Wu, S. H. & Zhang, J. J. (2009). *Int. J. Hydrogen Energy*, **34**, 388–404.